CHAPTER 7

LANTHANUM & MAGNESIUM SUBSTITUTED Y-TYPE BARIUM HEXAFERRITE (CO_2-Y); AS A MICROWAVE ABSORBER FOR EMI SHIELDING APPLICATION

7.1 Introduction

The lanthanum and magnesium substituted Y-type barium hexaferrite $Ba_{2-x}La_xCo_{2-x}Mg_xFe_{12}O_{22}$ (x = 0.0, 0.1, 0.2, 0.3, 0.4 & 0.5) are synthesized using the nitrate-based sol-gel auto combustion method and investigated its potential as an EMI shielding material in Ku-band frequency. The proposed hexaferrite samples are prepared using the analytical grades of barium nitrate [$Ba(NO_3)_2$], lanthanum nitrate [$La(NO_3)_3.6H_2O$], cobalt nitrate [$Co(NO_3)_3.6H_2O$], magnesium nitrate [$Mg(NO_3)_2.6H_2O$], ferrous nitrate [$Fe(NO_3)_3.9H_2O$], as elemental precursors and citric acid [$C_6H_8O_7{\cdot}H_2O$] as a chelating agent or fuel within the process.

To overcome the major issues, such as poor thermo-chemical stability, low ferromagnetic resonance frequency (FMR), expensive fabrication, narrow working range of temperature (low curie temperature), related to the largely utilized spinel-based ferrite and few hexaferrite systems. The Y-type $Ba_2Co_2Fe_{12}O_{22}$ ferrite are explored with several advantages likewise better thermos-chemical stability, excellent mechanical hardness, higher value of saturation magnetization, higher value of Curie temperature, wear and corrosion resistance, large uniaxial-magnetic anisotropy [(Pubby *et al.*, 2018), (Jotania and Virk, 2012), (Stergiou and Litsardakis, 2016), (Adeela *et al.*, 2016)].

Earlier studied ferrite systems inspired the selection of lanthanum as a substituting element at the barium site. The replacement of barium with lanthanum in Co_2Z-type hexaferrite results in improved magnetic losses and better absorbency within the 2-18 GHz region [(Xu *et al.*, 2009)]. The La^{3+} ions improve soft magnetic properties and behave as grain growth inhibitors in the hexaferrites compositions [(Xu *et al.*, 2009)]. A similar substitution within the M-type barium hexaferrite system results in an enhanced microwave absorbance, achieving a reflection loss value of -23.02 dB [(Li, Wang, and Wang, 2012)]. The substitution of Mg shows its utility as an effective dopant to increase the microwave

performance of M-Type barium hexaferrite, resulting in a better reflection loss value up to -63.85 dB (approx. 99.99% absorbance) at 10.90 GHz [(Rianna *et al.*, 2019)]. Substituting Mg within Y-type hexaferrite with replacing cobalt increases the saturation magnetization value of the system [(Alizad Farzin, Mirzaee, and Ghasemi, 2016)].

The as-prepared nano-crystalline Co_2-Y powders are analyzed using XRD and FTIR to study their structural variations. The calcined powders are mixed with three wt% poly-vinyl alcohol & pressed at about 6 tonnes per cm^2 pressure to obtain a rectangular-shaped (16 mm x 8 mm) compact for the Ku-band waveguide measurement. These pressed samples are sintered at 1050ºC for 2 hrs with a heating rate of 3ºC/min in the controlled muffle furnace. The structural properties using XRD and FTIR spectroscopy, morphological properties using SEM and EDS, thermomagnetic properties using SQUID-VSM, and Ku-band electromagnetic properties using VNA (to measure the scattering parameters (S_{11}, S_{21}, S_{12}, and S_{22}) are conducted extensively with the sintered samples.

7.2 Results and discussion

The indexed XRD patterns of the calcined ferrite powders with different La and Mg content are displayed in Fig.7.1. The peaks attained in the XRD are well-matched with the standard JCPDS file (Card no # 44-0206), which consists of the pure phase of $Ba_2Co_2Fe_{12}O_{22}$ ferrite with rhombohedral crystal and *R-3m* space group. All XRD patterns demonstrate well distinct (intense) and sharp diffraction peaks, which favor the formation of well-crystallized lanthanum and magnesium substituted Co_2Y-type hexaferrite. There is a slight variation in the position of the peaks due to the substituent concentration. The intensity of the peaks fluctuates to some extent from the reference peaks due to the deviation in the preferred orientation of hexagonal plates [(Mallick, Shepherd, and Green, 2007)]. The lanthanum ferrite ($LaFeO_3$) (JCPD card # 75-0541) and magnesium ferrite

($MgFe_2O_4$) (JCPD card # 71-1232) are detected as impurities with increasing the doping concentration after x = 0.1. The unit cell parameters, (*c/a*) ratio, unit cell volume along with crystallite size, and X-ray density of the calcined $Ba_{2-x}La_xCo_{2-x}Mg_xFe_{12}O_{22}$ ($0 \leq x \leq 0.5$) ferrite samples are calculated and shown in Table 7.1.

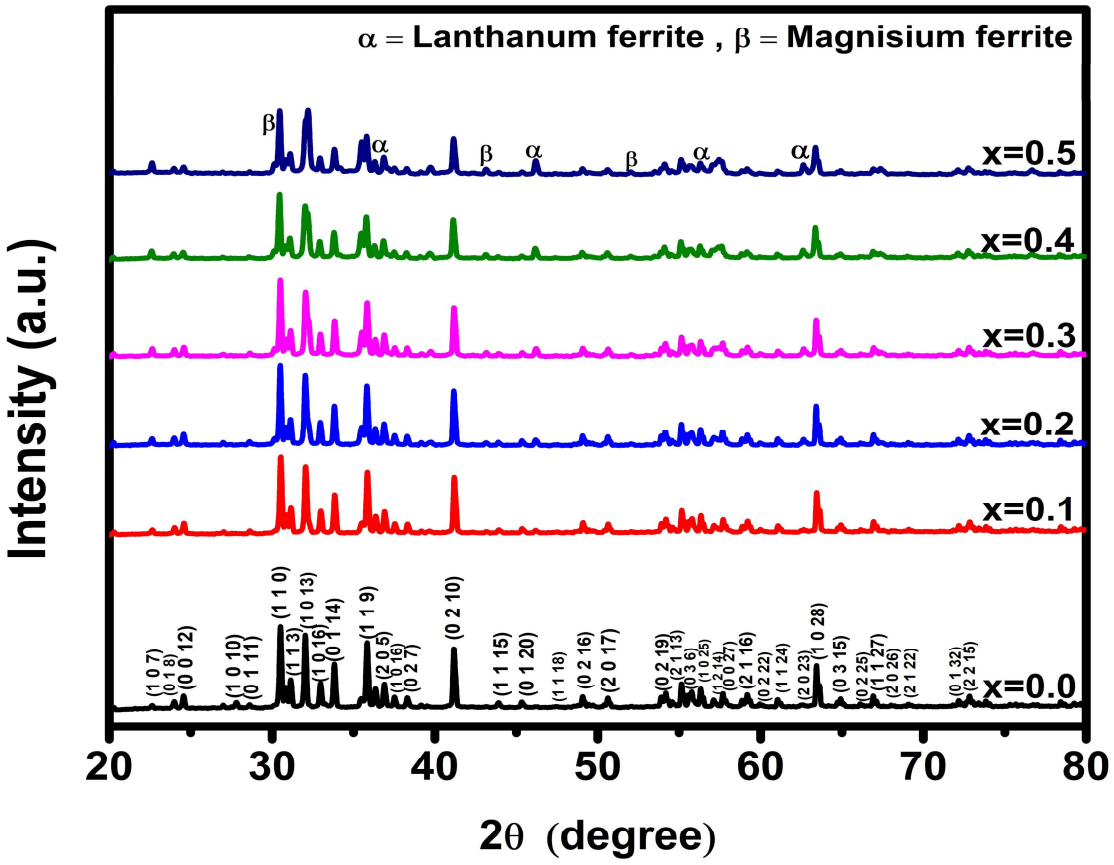

Figure 7.1 XRD patterns of calcined $Ba_{2-x}La_xCo_{2-x}Mg_xFe_{12}O_{22}$ ($0 \leq x \leq 0.5$) ferrite samples.

The smaller ionic size of La^{3+} (1.06 Å) has been substituted in place of the larger ionic size of Ba^{2+} (1.49 Å), and Mg^{2+} (0.720 Å) has been substituted in place of Co^{2+} (0.745Å) [(Kumar *et al.*, 2019), (Behera and Ravi, 2018)]. Therefore, the replacement of Ba^{2+} by La^{3+} and Co^{2+} by Mg^{2+} creates contraction of the unit cell. The XRD peaks are shifted towards the right side (higher 2θ value) with the increasing dopant (La^{3+} & Mg^{2+}) concentration in barium hexaferrite and owed to reducing the lattice parameters and cell

volume. The reduction in crystallite size with increasing the La and Mg content may be elucidated based on the ionic radii. The (*c/a*) ratio fluctuates from 7.419 to 7.425, which falls in the allowed range of Y-type hexagonal ferrites [(Chandel, Singh, Jasrotia, *et al.*, 2020)]. The unit cell volume and lattice parameters may be affected by the ionic radius of the exchanged metal ions. It reduces cell volume and lattice parameters up to x = 0.1; afterward, a slight increment in the unit cell is observed due to the mixed impact of both dopants and the formation of larger Fe^{2+} ions in the matrix. It is assumed that one La^{3+} ion is substituted with one Ba^{2+} ion and it (Ba^{2+} + Fe^{3+}) forms (La^{3+} + Fe^{2+}) [(Frantsevich and Tul'chinskii, 1971)]. It is well recognized that the ionic radius of Fe^{3+} and Fe^{2+} are 0.64 and 0.76 Å correspondingly; hence the greater *a* and *c* values may be shown due to the larger amount of Fe^{2+} ions [(Xu *et al.*, 2009)]. A decreasing trend in the value of X-ray density (D_x) is observed. It may be due to the smaller atomic mass of lanthanum and magnesium compared to barium and cobalt and the counter relation of unit cell volume.

Table 7.1 The unit cell parameters, crystallite size, and X-ray density of the calcined $Ba_{2-x}La_xCo_{2-x}Mg_xFe_{12}O_{22}$ ($0 \leq x \leq 0.5$) ferrite samples.

Composition	Lattice parameters		*c/a*	Volume (Å^3)	Crystallite size (nm)	X-ray density (g/cm^3)
	a (Å)	*c* (Å)				
x = 0.0	5.857	43.486	7.425	1291.904	94.47	5.45
x = 0.1	5.852	43.447	7.424	1288.543	90.48	5.45
x = 0.2	5.853	43.443	7.422	1288.925	87.40	5.44
x = 0.3	5.854	43.445	7.421	1289.305	85.69	5.43
x = 0.4	5.854	43.446	7.422	1289.365	82.80	5.41
x = 0.5	5.855	43.437	7.419	1289.568	80.35	5.40

Fourier transform infrared spectroscopy (FTIR) of all the calcined powders is performed at room temperature to elucidate the structural and chemical bonding variations in $Ba_{2-x}La_xCo_{2-x}Mg_xFe_{12}O_{22}$ ($0 \leq x \leq 0.5$) ferrite samples.

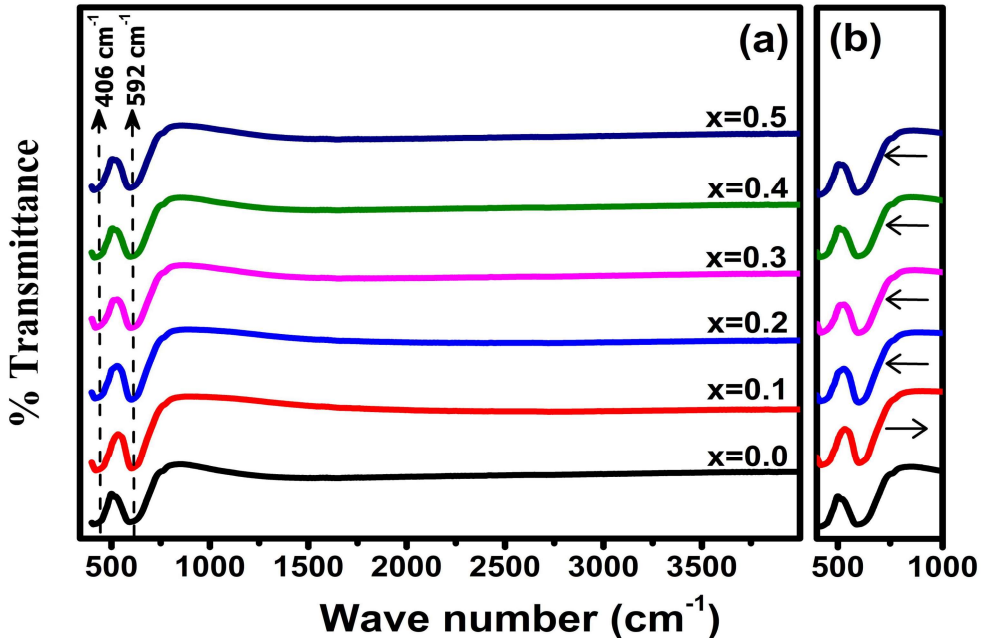

Figure 7.2 (a) FT-IR spectra, and (b) magnified view of shifting absorption band of calcined $Ba_{2-x}La_xCo_{2-x}Mg_xFe_{12}O_{22}$ ($0 \leq x \leq 0.5$) ferrite samples.

Fig. 7.2(a) demonstrates the FTIR spectrum of the lanthanum and magnesium substituted Y-type barium hexaferrite. It reveals two foremost absorption bands in the range 400 cm^{-1} and 600 cm^{-1} for all the samples. It resembles the metal cations' asymmetric stretching vibrational behavior at octahedral and tetrahedral lattice sites [(Salunkhe, Choudhary, and Kondawar, 2013)]. The low-frequency band around 400 cm^{-1} (υ_2) and high-frequency band around 500 to 600 cm^{-1} (υ_1) are the mutual depictions of spinel ferrite structure. In a hexagonal system, these bands are accredited to cationic vibrations existing in the spinel block of Y-type ferrite [(Adeela *et al.*, 2016)]. The force constant associated with the Fe-O bond, along with respective bond length values, are calculated and tabulated in Table 7.2.

Table 7.2 Wave number, effective mass, force constant, and bond length of the calcined $Ba_{2-x}La_xCo_{2-x}Mg_xFe_{12}O_{22}$ ($0 \leq x \leq 0.5$) ferrite samples.

Composition	Wave number (cm^{-1})	Effective mass (10^{-26} kg)	Force constant (N/cm)	Bond length (Fe–O) (Å)
x = 0.0	592.122	2.065	2.571	1.876
x = 0.1	601.766	2.065	2.656	1.856
x = 0.2	599.837	2.065	2.639	1.860
x = 0.3	597.909	2.065	2.622	1.864
x = 0.4	595.979	2.065	2.605	1.868
x = 0.5	594.051	2.065	2.588	1.872

The absorption peak associated with the tetrahedral site (υ_1) has a higher wavenumber corresponding to its octahedral characteristics peak (υ_2) due to the shorter bond length [(Kulkarni and Mathad, 2019)]. It has been noticed that initially, the addition of dopants shifts υ_1 towards a higher wavenumber, as shown in Fig. 7.2.(b). This steady shift of these bands towards the right can be accompanied by the replacement of a larger cation with a smaller cation, which describes the contraction of the unit cell. Afterward, it follows a slight shifting towards the lower wavenumber, which also confirms the volumetric expansion of the unit cell similar to XRD results [(Kunwar *et al.*, 2019)].

Table 7.3 shows the bulk density along with percentage porosity and grain size of the sintered $Ba_{2-x}La_xCo_{2-x}Mg_xFe_{12}O_{22}$ ($0 \leq x \leq 0.5$) ferrite samples**.** It can be perceived that the bulk densities measured by the Archimedes principle are lower than that of X-ray densities, as shown in Table 7.1. It is anticipated due to the existence of unavoidable pores created during the sintering process [(Irfan *et al.*, 2014)]. In contrast, the percentage porosity increases from 23.92 to 31.24. It may be due to the addition of Mg^{2+} content, which decreases X-ray density, and various distortions arise with dissimilarity in atomic radii of the host and dopant ions [(Adeela *et al.*, 2016), (Zhang *et al.*, 2016)].

Table 7.3 Values of bulk density, percentage porosity, and grain size of the sintered $Ba_{2-x}La_xCo_{2-x}Mg_xFe_{12}O_{22}$ ($0 \leq x \leq 0.5$) ferrite samples.

Composition	Bulk density (g/cm^3)	Percentage Porosity (%)	Grain Size (μm)
x = 0.0	4.15	23.92	2.19
x = 0.1	4.09	24.90	1.78
x = 0.2	4.03	25.86	1.58
x = 0.3	4.01	26.13	1.41
x = 0.4	3.83	28.85	1.39
x = 0.5	3.71	31.24	1.37

The exploration of microstructure becomes vital as the micro-structural sorts like grain size and porosity affect the characteristics of the hexaferrites. Fig.7.3 displays the surface morphologies along with EDX analysis of the sintered hexaferrite pellets. The difference in morphological microstructure is visible in terms of shape, porosity, and grain size. The EDX analysis confirms the desired elements, likewise Ba, La, Co, Mg, Fe, & O, in the samples with no impurity. The scanning electron micrographs illustrate that substituted barium hexaferrite up to x = 0.1 shows nearly hexagonal-shaped grains with enhanced porosity [(Rianna *et al.*, 2019), (Chandel, Singh, Singha, *et al.*, 2020)], supporting the structural analysis. A higher amount of La and Mg (x = 0.2-0.5) samples show a duplex grain structure with wide grain size distribution due to the formation of small impurity phases like lanthanum ferrite and magnesium ferrite near the grain boundaries. The average grain size, calculated using the line method, shows a continuous decreasing trend in the range of 2.19 μm to 1.37 μm.

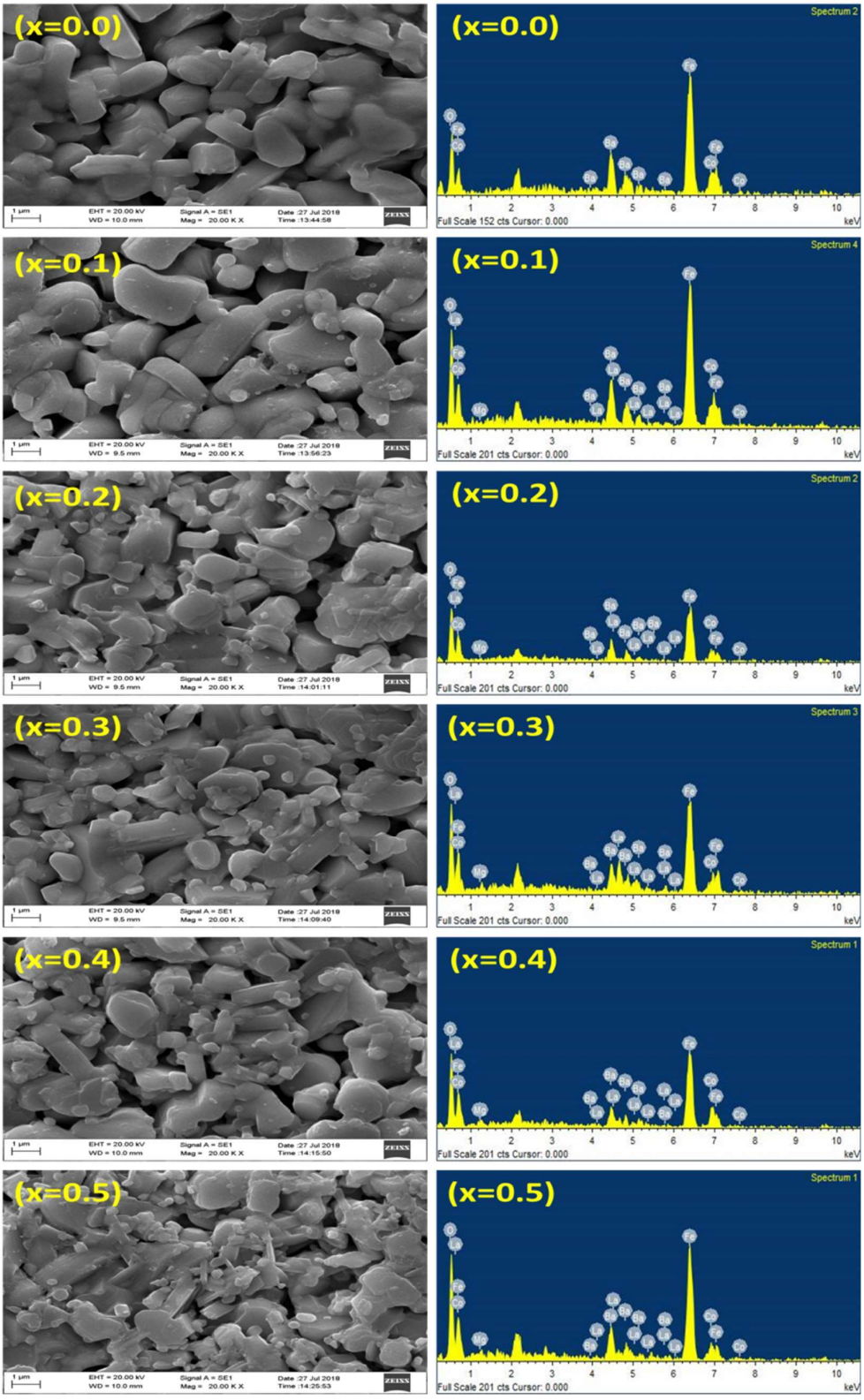

Figure 7.3 SEM micrographs along with EDX spectra of sintered

$Ba_{2-x}La_xCo_{2-x}Mg_xFe_{12}O_{22}$ ($0 \leq x \leq 0.5$) ferrite samples.

The decreasing grain size trend (Table 7.3) can be explained by the dominating role of lanthanum amount or the presence of secondary phases, which act as a grain growth inhibitor and retard the grain boundary movement [(Xu *et al.*, 2009), (Chang, Feng and Chen, 2009)]. Subsequently, the critical size of the single-domain was reported to be about 1.18 μm [(Hosseinkhan Nejad, Farzin, and Heydari, 2017)] in Y-type hexaferrite; it may be accomplished that the synthesized samples consist of multi-domain grains. The elemental mapping of the sample $Ba_{1.5}La_{0.5}Co_{1.5}Mg_{0.5}Fe_{12}O_{22}$ (shown in Fig. 7.4) confirms the segregation of dopants (both La & Mg), owing to the formation of lanthanum and magnesium-rich secondary phases within the matrix.

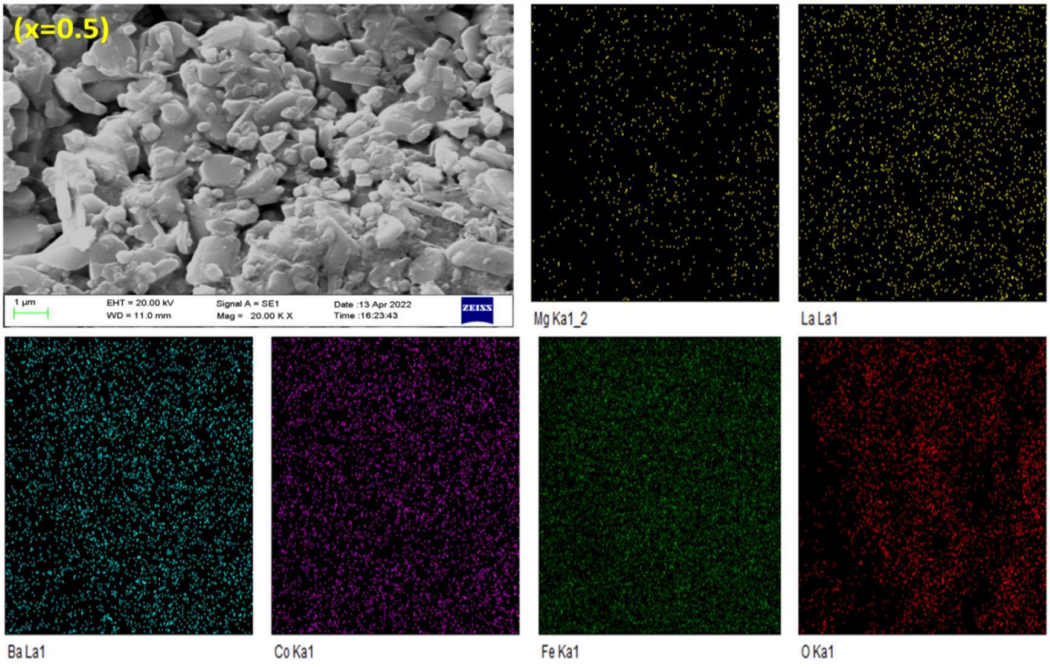

Figure 7.4 SEM micrograph along with elemental mapping obtained using EDX analysis of $Ba_{1.5}La_{0.5}Co_{1.5}Mg_{0.5}Fe_{12}O_{22}$ ferrite sample.

The room temperature *M-H* curves (up to an applied magnetic field of ±20 kOe) of the sintered $Ba_{2-x}La_xCo_{2-x}Mg_xFe_{12}O_{22}$ ($0 \leq x \leq 0.5$) ferrite samples are shown in Fig. 7.5. All the samples show magnetic hysteresis loops, which comprise a strong ferromagnetic

behavior in Y-type barium hexaferrite. It is found that the magnetization does not find to be saturated perfectly under the maximum applied field (±70 kOe) of the instrument. Therefore, it is compulsory to explore it using the law of approach to measure magnetic saturation with the Stroner–Wohlfarth (S–W) model (shown in Fig. 7.6). All the derived parameters such as saturation magnetization (M_s), remnant magnetization (M_r), number of Bohr magneton, squareness ratio (M_r/M_s), coercivity field (H_c), anisotropy field (H_a), and magnetic anisotropy constant (K_1) are calculated and tabulated in Table 7.4.

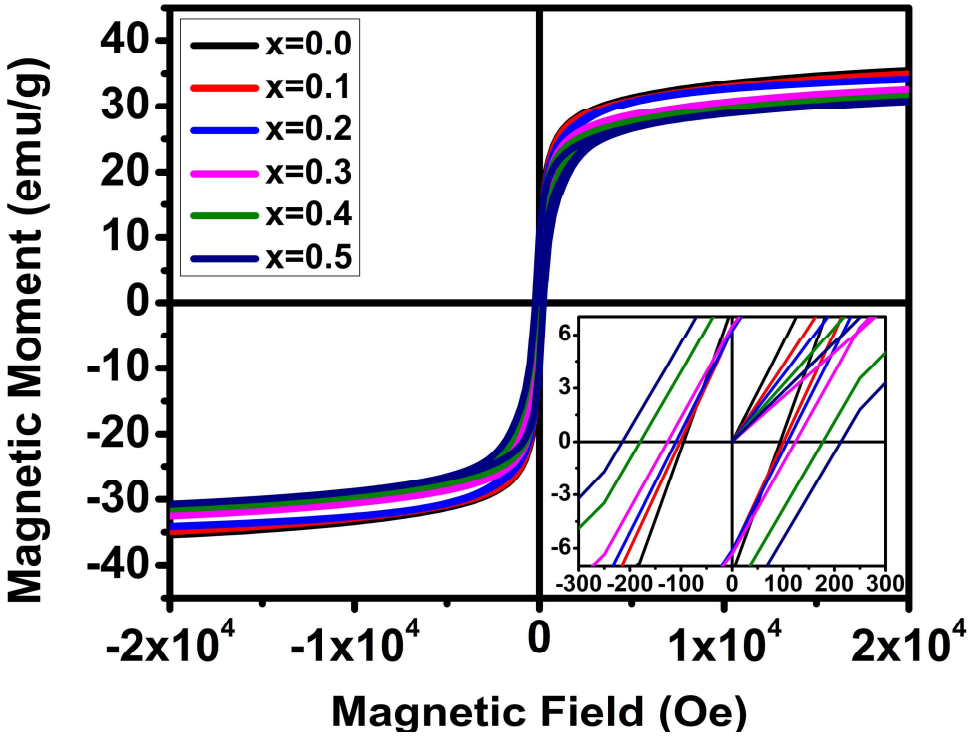

Figure 7.5 Room temperature hysteresis loops of sintered $Ba_{2-x}La_xCo_{2-x}Mg_xFe_{12}O_{22}$ ($0 \leq x \leq 0.5$) ferrite samples.

It can be understood from Table 7.4 that the value of saturation magnetization (M_s) decreases continuously from 38.53 emu/g to 33.71 emu/g with increasing La and Mg content. The magnetization phenomenon can be explained based on several factors, such

as the interaction of super-exchange strength (Fe^{3+}–O–Fe^{3+}), the phenomenon of spin-canting, and magnetic dilution of valance-state charges of Fe^{3+} ($3d_5$ at high-spin) ions into Fe^{2+} ($3d_6$ at low-spin) [(Anjum, Seher, and Mustafa, 2019)]. In the unsubstituted sample (x = 0.0), it is obvious to place these ions according to their size. The larger ion Ba^{2+} (1.49 Å) acquires an octahedral position, and the smaller ion Fe^{3+} (0.68 Å) remains for the tetrahedral site. It is known that the Ba^{2+} ion does not provide any magnetic moment contribution to the system, so the magnetization belongs to uncompensated ferric ions only [(Anjum, Seher, and Mustafa, 2019)].

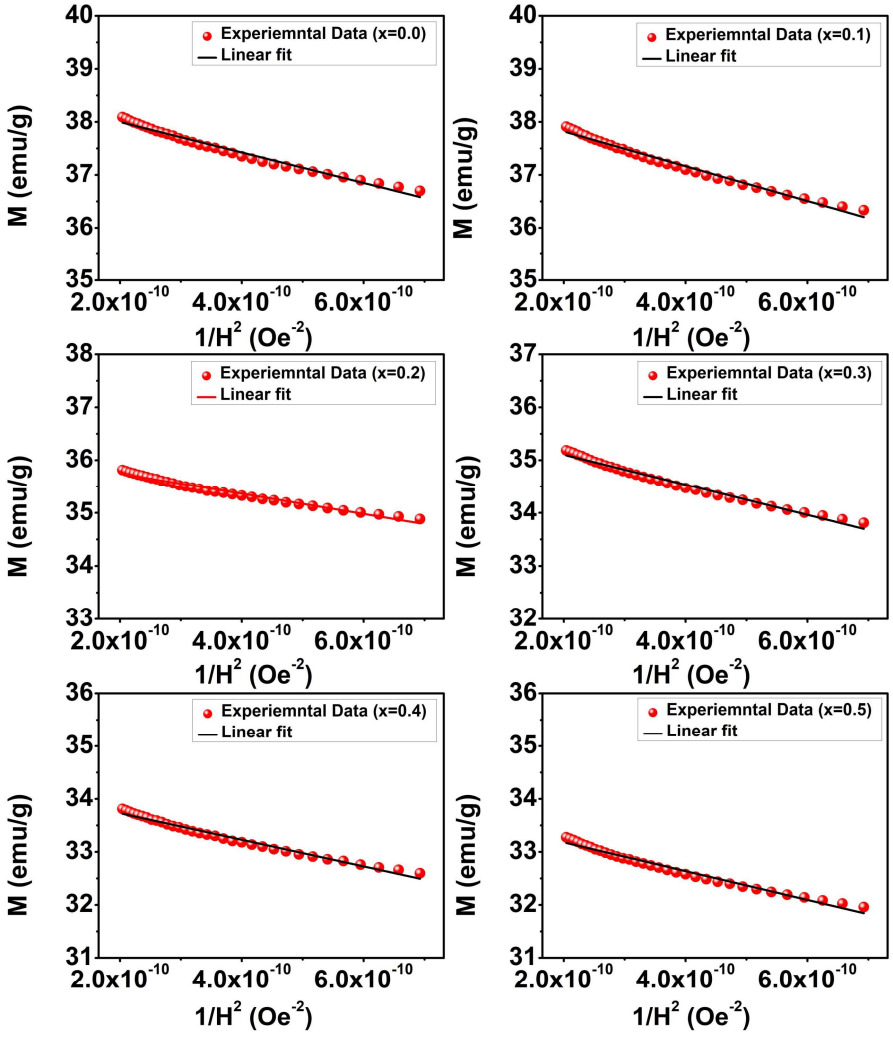

Figure 7.6 Magnetization vs. $1/H^2$ curves of sintered $Ba_{2-x}La_xCo_{2-x}Mg_xFe_{12}O_{22}$ ($0 \leq x \leq 0.5$) ferrite samples.

Table 7.4 The saturation magnetization (M_s), remnant magnetization (M_r), number of Bohr magneton (N_{BM}), squareness ratio (M_r/M_s), coercivity (H_c), anisotropy field (H_a), and magnetic anisotropy constant (K_1) of the sintered $Ba_{2-x}La_xCo_{2-x}Mg_xFe_{12}O_{22}(0 \leq x \leq 0.5)$ ferrite samples.

Composition	M_s (emu/g)	M_r (emu/g)	N_{BM}	M_r/M_s	H_c (Oe)	H_a (kOe)	K_1 (erg/Oe)
x = 0.0	38.53	7.53	9.76	0.195	94.17	26.80	3779.55
x = 0.1	38.37	6.20	9.70	0.162	100.94	27.70	4034.45
x = 0.2	36.27	6.25	9.14	0.172	109.14	28.50	4123.44
x = 0.3	35.61	6.49	8.96	0.182	124.74	28.70	4627.07
x = 0.4	34.27	8.82	8.60	0.257	178.29	28.80	6364.58
x = 0.5	33.71	10.38	8.44	0.308	213.30	31.30	7489.94

With the substitution of La^{3+}ions into the system, some of the Fe^{3+} ions convert to the Fe^{2+} ion to make charge neutrality and lower the super-exchange interaction (from Fe^{3+}–O–Fe^{3+} to Fe^{3+}–O–Fe^{2+}.), resulting in the reduction of magnetization [(Anjum, Seher, and Mustafa, 2019), (Ounnunkad, 2006)]. The decreasing value of saturation magnetization (M_s) can also be explained on behalf of the replacement of a magnetic ion Co^{2+} (having a magnetic moment of 3.88 μ_B per ion) with a nonmagnetic ion Mg^{2+} [(Behera and Ravi, 2018)]. Other reasons to decrease the M_s may be the formation of cationic vacancies, and several environmental disorders, which disturb the collinear ferromagnetic order due to the substitution [(Thakur, Singh, and Barman, 2013)]. With the higher doping level, the decrease of M_s may be due to the formation of secondary phases, like $LaFeO_3$ (M_s - 0.17 emu/g, calcined at 1000˚C) and $MgFe_2O_4$ (M_s - 20.45 emu/g calcined at 1100˚C) with lower M_s values, as reported earlier [(Manikandan, Manimuthu, and Venkateswaran, 2014), (Hessien *et al.*, 2017)].

The remanence (M_r) informs about the magnetization held within the sample after removal of the external applied magnetic field ($H = 0$). It can be observed that the value of M_r decreases up to x = 0.1, and later it increases with further doping addition. Generally, on hard ferrite materials, the value of M_r needs to follow the similar trend of the M_s, but sometimes the trend may deviate from its expected values [(Ali *et al.*, 2013), (Ali *et al.*, 2014)]. Usually, the remanence magnetism of hard ferrite material depends on the sample density, elemental chemistry, and orientation to the applied magnetic field [(Ali *et al.*, 2013)]. As the density and elemental chemistry of the substituted sample does not support the increasing behavior of M_r, it may be considered due to the increasing orientation of the preferred magnetization plane towards the direction of the externally applied field. It can alter the M_r value of the sample without concern for the overall M_s and H_c [(Zhang *et al.*, 2014)]. It is known that the Y-type hexaferrites are ferroxplana, having an easy direction of magnetization within the hexagonal basal plane itself or in a right circular cone at an angle to the *c*-axis. The ideal plane of magnetization is free to switch within the Basel-plane or cone. The magneto-crystalline anisotropy field (H_a) is sufficient to move its plane or cone of magnetization within hexaferrite samples. The value of the anisotropy field (Table 7.4) increases with the substitution level. The abnormal behavior of the remanence is observed because the preferred plane or cone of the magnetization has more tendency to align towards the externally applied field [(Pullar, 2012)].

The squareness ratio is significant to accomplish the order of magnetic hardness of any material. This ratio, which varies from 0 to 1, defines the existence or deficiency of various types of intergranular group exchanges for that particular material. The squareness ratio for all the samples lies in the range of $0.05 < M_r/M_s < 0.5$, which indicates a pseudo-single domain structure where a fraction of magnetization processes are controlled by the

movement of the magnetic domain-wall rather than by rotational magnetization [(Adeela *et al.*, 2016)].

The coercivity (H_c) value is enhanced continuously because of the replacement of Ba^{2+} ions with La^{3+}ions, which results in the formation of Fe^{2+} ions into the structure. It ensures the larger magneto-crystalline anisotropy and H_c [(Ounnunkad, 2006), (Sorlateap and Keawwattana, 2013)], suppression of ferromagnetic order by the presence of paramagnetically ordered La^{3+} ion to the structure [(Anjum, Seher, and Mustafa, 2019)]. It may be due to the presence of secondary phases, which have higher coercivity values (335 Oe and 249.28 Oe for magnesium and lanthanum ferrite, respectively) as compared to base material [(Manikandan, Manimuthu, and Venkateswaran, 2014), (Hessien *et al.*, 2017)]. It may also be due to the smaller grain size (Table 7.3) of the matrix. It has been stated that the coercivity value (H_c) increases with reducing the grain size within a multi-domain ferrite system [(Singhal *et al.*, 2010)]. This disparity of H_c can be elucidated based on domain structure, anisotropy of the crystal, domain wall energy, and the critical diameter. It is also found in Table 7.4 that the magneto-crystalline anisotropy constant (K_1) values are in good agreement with the value of coercivity (H_c) and grain size. As earlier reported that the incorporation of La and Mg in the barium hexaferrite enhances the anisotropy constant (K_1) due to the formation of Fe^{2+} ions or the presence of nonmagnetic elements in the magnetic network [(Anjum, Seher, and Mustafa, 2019)].

The thermomagnetic (both ZFC and FC magnetization curves) curves, measured between a temperature range of 2 K to 300 K at a fixed applied field of 300 Oe, along with their derivatives (Derivative Y1 = dM/dT) of the $Ba_{2-x}La_xCo_{2-x}Mg_xFe_{12}O_{22}$ ($0 \leq x \leq 0.5$) ferrite samples sintered at 1050ºC present in Fig. 7.7. The magnetization curves of $x = 0.0$ composition clearly indicate the presence of a single magnetic Y-type barium hexaferrite phase, along with the presence of Hopkinson peak below the Curie temperature (613 K for

$Ba_2Co_2Fe_{12}O_{22}$) [(Koutzarova *et al.*, 2019)]. The existence of the Hopkinson peak attributes to the presence of a minor fraction of particles having super-paramagnetic nature in the samples. As the substitution level increases the Hopkinson peak gets minimized due to the lowering super-paramagnetic fraction or increased value of magnetic anisotropy constant (Hopkinson peak height $\propto K_1^{-1/2}$) [(Mahmood *et al.*, 2017)]. It is also revealed that all the synthesized samples display a paraelectric nature without an applied magnetic field. The transition temperatures (inflection point) determined from the first derivative of the ZFC magnetization curves near 110 K (indicated by an upward arrow) and 210 K (indicated by a downward arrow) provide information about the magnetic phase transitions from a ferrimagnetic to a helical spin order.

These transitions are accountable for explaining the multiferroic properties of this material [(Tae Lim and Sung Kim, 2014)]. The results obtained in the synthesized samples are in good agreement with the earlier reported values for these inflection points. *Wu et al.* have stated that in the case of Y-type barium ($Ba_2Mg_{0.4}Co_{1.6}Fe_{12}O_{22}$) hexaferrite, the magnetic arrangement converts from a collinear ferrimagnetic nature to a proper screw spin order around 226 K with lowering the temperature in the absence of any magnetic field. It is also noticed that there is another transition (near 92 K) due to a longitudinal-conical spin arrangement, where the ferromagnetic moment offers the possibility for adjusting the electrical polarization in a small magnetic field applied along the (001) plane [(Koutzarova *et al.*, 2019), (Wu *et al.*, 2016)].

Electromagnetic properties for all the samples are considered by measuring complex permeability and permittivity in the frequency range of 12.3-17.5 GHz (Ku-band). Microwave absorbing materials functioning at a frequency range of 12.3–17.5 GHz can efficiently absorb electromagnetic waves and disperse the electromagnetic waves by interfering with or converting energy into thermal energy. The samples used for

electromagnetic characterization are sintered in a rectangular compacted shape (15.8 mm X 7.9 mm) with nearby equal thickness. Complex permittivity ($\varepsilon = \varepsilon' - i\varepsilon''$) and permeability ($\mu = \mu' - i\mu''$) is signified by the dielectric and magnetic belongings of the samples, respectively.

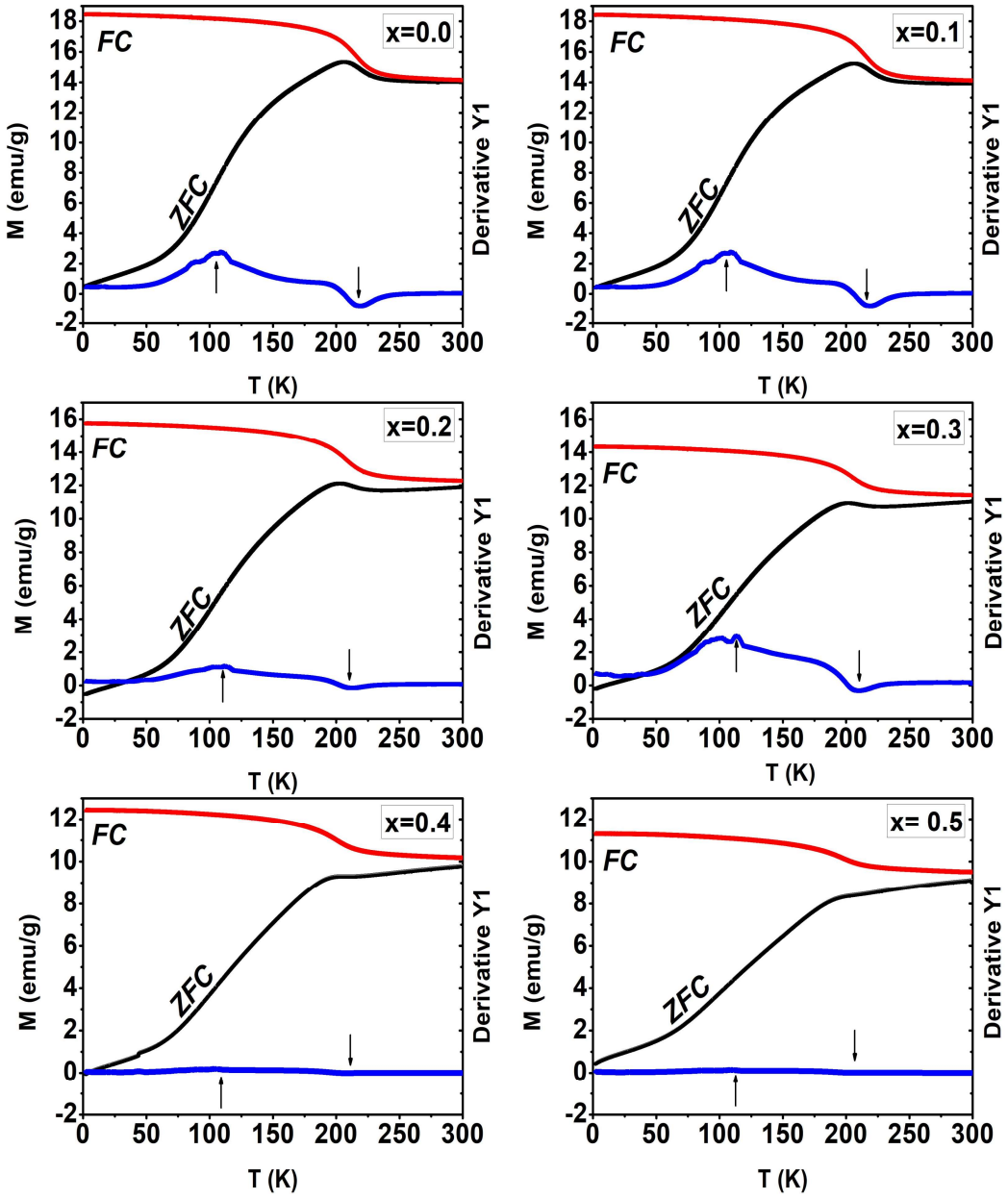

Figure 7.7 Thermo-magnetic curves (both FC, ZFC) & first-order derivative of magnetization (the lowermost curve with blue line) of sintered $Ba_{2-x}La_xCo_{2-x}Mg_xFe_{12}O_{22}$ ($0 \leq x \leq 0.5$) ferrite samples at an applied field of 300 Oe.

The real part is attached to the storage proficiency of magnetic and electric energies, and the imaginary parts are assigned for the losses affiliated with these energies [(Nikmanesh, Hoghoghifard, and Hadi-Sichani, 2019)]. The experimental outcomes show that the superior microwave absorption is primarily because of the elucidated magnetic losses and the distinctive microstructure [(Wu, Wu, and Wang, 2015)]. Fig. 7.8 demonstrates frequency-dependent performance of the real and imaginary part of permittivity of the samples in the Ku-band of frequency (12.3–17.5 GHz). The electromagnetic properties, along with the shielding parameters at different frequencies, are shown in Table 7.5. The ε′ of the samples gradually varies, whereas ε″ is close to unity on average, signifying the weak dielectric loss of the barium hexaferrite. In the Ba-hexaferrite, the cations contribute the ε′ and ε″ through relaxation of dipole and dipolar polarization [(Nikmanesh, Hoghoghifard, and Hadi-Sichani, 2019)].

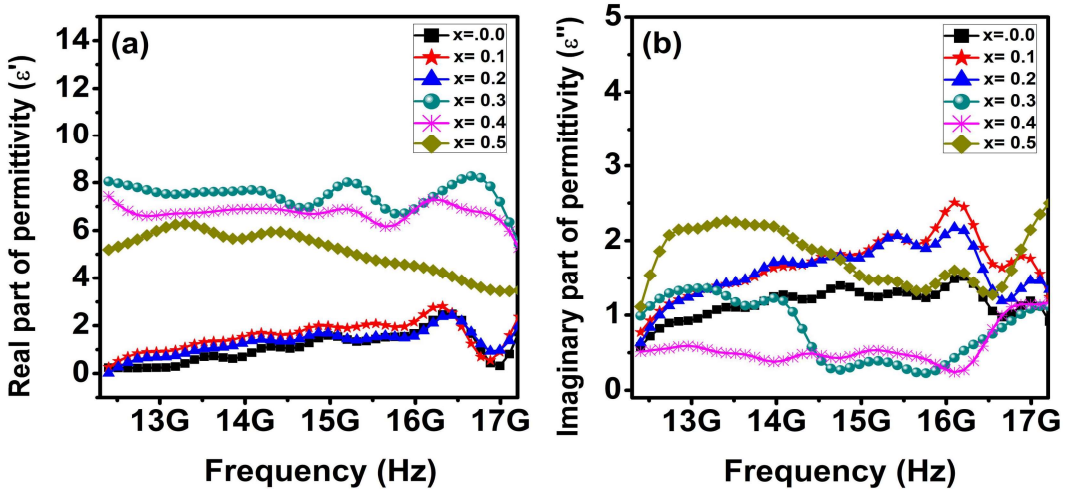

Figure 7.8 Frequency dependency (a) real and (b) imaginary part of complex permittivity of sintered $Ba_{2-x}La_xCo_{2-x}Mg_xFe_{12}O_{22}$ ($0 \leq x \leq 0.5$) ferrite samples.

On the other hand, when the barium is replaced by lanthanum and cobalt is replaced with magnesium, dipoles of different magnitude are obtained. It may be a reason for the

slight change or increment of the value of ε′ and ε″, respectively. The ε′ differs from (0.23 - 2.22) for x = 0.0 and is found to be increased with the doping of cations. The real part of permittivity increases (up to x = 0.3) with a maximum value of 8.30 at 15.3 GHz, then it decreases with a higher content of doping. The imaginary part of complex permittivity shows a random behavior for all the values of x in the range of 0.28 for x = 0.2 at 14.6 GHz to 2.50 for x = 0.1 at 16.1 GHz. This variation in the permittivity values can be explained in support of increased magneto-crystalline anisotropy, or variation in electronic, ionic, and interfacial polarization within the samples [(Shams Alam *et al.*, 2016), (Rana *et al.*, 2018)]. The dielectric behavior of the ferrite sample at higher frequencies may be explained by the inherent electric dipole polarization and interfacial polarization. The incorporation of La^{3+} results in converting some Fe^{3+} ions into Fe^{2+} ionic states to maintain electrical-charge neutrality. It also enhances the phenomena of electron hopping between Fe^{3+} and Fe^{2+}. As reported earlier, the more the number of Fe^{2+} ions in the sample leads to more surface polarization due to local charge imbalance, resulting in a higher permittivity value in the substituted samples [(Frantsevich and Tul'chinskii, 1971),(Stergiou and Litsardakis, 2011), (Mosleh *et al.*, 2016)].

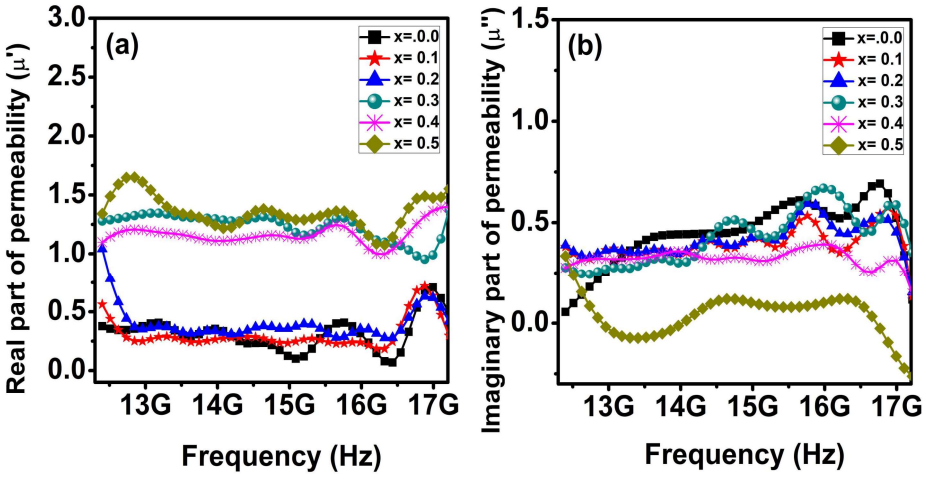

Figure 7.9 Frequency dependency (a) real and (b) imaginary part of complex permeability of sintered $Ba_{2-x}La_xCo_{2-x}Mg_xFe_{12}O_{22}$ ($0 \leq x \leq 0.5$) ferrite samples.

Fig 7.9 shows the frequency-dependent performance of the real and imaginary part of permeability for different substitutions. It is revealed that the real part of permeability (μ′) is increased with a maximum value of 1.65 for x = 0.5 (at 12.84 GHz) in the Ku-band. The real part of permeability shows no abnormal variation in the scanned frequency region. The greatest value of the μ′ can be understood by the existence of secondary phases with higher permeability values in x = 0.5 composition. The natural ferromagnetic resonance (FMR) and the domain wall resonance are generally accountable for the magnetic losses in a multi-domain magnetic material. The domain wall resonance is more effective at lower frequencies, about 1 to 100 MHz. Normally, the natural FMR value for Y-type barium hexaferrite is dependent on the anisotropic field (H_a) and is found around 18 GHz or higher frequency [(Shams Alam *et al.*, 2016), (Harris *et al.*, 2014)]. Generally, the resonance frequency for a polycrystalline ferrite sample with randomly oriented easy axes is followed Snoek's relation [(Mosleh *et al.*, 2016)];

$$f_{resonance} = \xi.\frac{2K_1}{M_S} = \xi.H_a \qquad (7.1)$$

Where ξ is the gyromagnetic ratio, K_1 and H_a represent the anisotropy constant and anisotropy field, respectively. The magnetic loss of barium hexaferrite at the microwave frequency region is expressed as;

$$\mu'' = \left(1/\zeta\right).\left(M_s/2H_a\right) \qquad (7.2)$$

Where ζ is the extinction coefficient, it can be understood that the increasing value of the anisotropy field of the synthesized samples is responsible for shifting the ferromagnetic resonance frequency towards a higher frequency range beyond the instrument's limit. So, no abnormal magnetic loss behavior is shown in the synthesized samples within the scanned frequency range. The decreasing magnetic losses with the addition of La^{3+} and Mg^{2+} may be due to the increasing anisotropy field (H_a) in the samples [(Mosleh *et al.*, 2016)].

Microwave properties of any hexaferrite materials are measured using scattering parameters, primarily expressed as S_{11} and S_{21}, obtained using VNA. The S_{11} parameter describes the reflecting behavior of the surface, whereas the S_{21} parameter represents the transmission behavior of the microwave through the material. A higher value of the S_{11} parameter indicates a higher reflection, and similarly, a lower S_{21} value resembles lower transmission and more shielding properties. When electromagnetic radiation is exposed to a specimen, a part of the EM radiation is reflected, a part is absorbed into it, and the residual is transmitted. The reflection loss (R_L) is generated due to a mismatch of impedance between the sample and free space [(Joseph *et al.*, 2013)]. Usually, a specimen with the least reflection and attenuation of transmitted wave possesses high shielding ability [(Chandra Babu Naidu, Roopas Kiran, and Madhuri, 2017)]. For any material, the total effectiveness of EMI shielding (SE_T) can be understood with a combined influence of all three factors, i.e., shielding effectiveness due to absorption (SE_A), shielding effectiveness due to reflection (SE_R), and shielding effectiveness due to multiple reflective (SE_M). Thus, $SE_T = SE_R + SE_A + SE_M = -\log (P_T/P_I)$, where "$P_T$" is the power transmitted and "P_I" is the power incident. The third factor (SE_M) for EMI shielding can be neglected due to inappropriate quantification as a separate factor. Hence, SE_T can be stated as $SE_T = SE_R + SE_A$. These two terms are calculated using the following equations [(Li *et al.*, 2021), (Pal *et al.*, 2021)]:

$$SE_R = -10 \log (1 - R), \text{ where } R = |S_{11}|^2 = |S_{22}|^2 \quad (7.3)$$

$$SE_A = -10 \log[T_s/(1 - R)], \text{ where } T_s = |S_{12}|^2 = |S_{21}|^2 \quad (7.4)$$

Where "T_s" and "R" resemble the transmissivity and reflectivity of incident radiation, respectively. In equations (7.3) and (7.4), the scattering parameters S_{11} and S_{21} are measured using VNA.

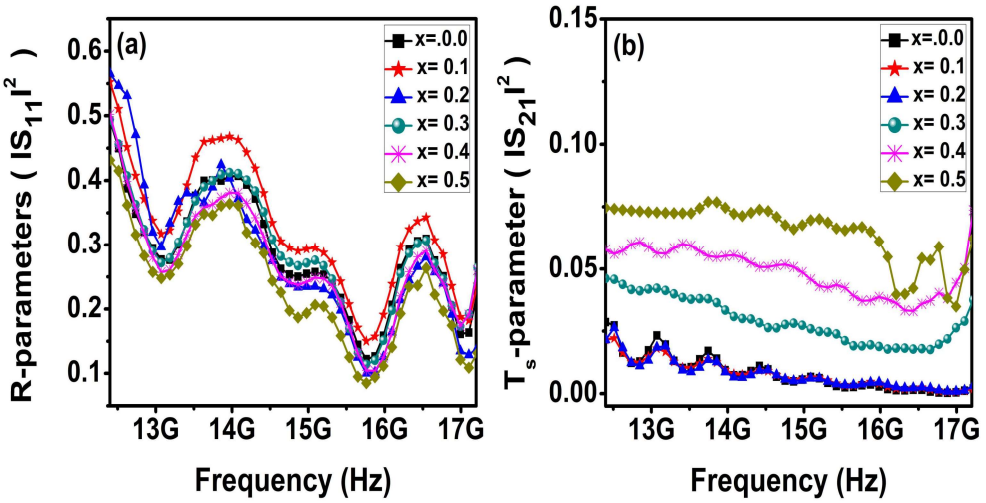

Figure 7.10 Frequency dependence of (a) R-parameter (reflectivity) and (b) T_s-parameter (transmissivity) of sintered $Ba_{2-x}La_xCo_{2-x}Mg_xFe_{12}O_{22}$ ($0 \leq x \leq 0.5$) ferrite samples.

Fig. 7.10 (a) and (b) demonstrate the R-parameter ($lS_{11}l^2$) and T_s-parameter ($lS_{21}l^2$) as a function of the frequency of sintered $Ba_{2-x}La_xCo_{2-x}Mg_xFe_{12}O_{22}$ ($0 \leq x \leq 0.5$) ferrite samples. It can be understood from the R– f curves that these samples display similar trends with frequency, and all substituted samples have higher values than pure barium hexaferrite. The x = 0.5 composition shows the lowest obtained R values (0.085) at 15.7 GHz. On the other hand, T_s-parameter is gradually increased with increasing the La^{3+} and Mg^{2+} levels. The x = 0.5 composition shows the maximum obtained R values (0.55) at 12.5 GHz. The T_s-parameter increases with increasing the doping level and reaches the highest value of 0.093 at 12.5 GHz for x = 0.5 composition.

Fig. 7.11 shows the frequency-dependent behavior of reflective shielding effectiveness (SE_R), absorptive shielding effectiveness (SE_A), total shielding effectiveness (SE_T), attenuation coefficient (ξ), ac conductivity, and reflection losses of sintered $Ba_{2-x}La_xCo_{2-x}Mg_xFe_{12}O_{22}$($0 \leq x \leq 0.5$) ferrite sample. Normally, all these parameters justify the electromagnetic absorption behavior of these samples. Generally, the EMI shielding is

determined by the attenuation of EM radiation. The reflective shielding efficiency of any material shows dependency on the mobile-charge carriers, which affiliate with the incident EM wave. In the case of absorptive shielding efficiency, it is dependent on the electrical or magnetic dipole and thickness of the shield [(Kashi *et al.*, 2016)]. *Wang et al.* have stated that these shielding efficiencies can be described by electrical conductivity or magnetic permeability [(Wang *et al.*, 2016)]. Analyzing Fig 7.11 (a) and (b), it can be assumed that the value of reflective shielding effectiveness (SE_R) and absorptive shielding effectiveness (SE_A) are in reverse trend with frequency. These trends are in good agreement for barium hexaferrite with the earlier reported results [(Zahari *et al.*, 2016)]. The values of SE_R, SE_A, and SE_T at different frequencies are shown in Table 7.5. At 16.5 GHz, the SE_R values vary from 1.33 dB to 1.61 dB, and SE_A values display from 11.32 dB to 26.55 dB. These results suggest that the absorption mechanism dominates the total shielding efficiency compared to reflection. The resonating behavior of SE_A may be due to the electronic motion among the dipoles within applying electromagnetic field. As the frequency increases, it induces extra polarizations, which results in enrichment in absorption attenuation [(Chandra Babu Naidu, Roopas Kiran, and Madhuri, 2017)]. Fig. 7.11(c) shows the increasing trend of total shielding efficiency along with frequency. It can be explained due to the presence of porosity (Table 7.3) in the synthesized sample or maybe similar ac conductivity behavior [(Ahmed *et al.*, 2020)], as displayed in Fig. 7.11(e). The lowest numerical value for SE_T is found with x = 0.5 composition. It shows the highest total shielding efficiency among all the synthesized samples, with 11.30 dB at 12.5 GHz, 11.35 dB at 14.5 GHz, and 12.65 dB at 16.5 GHz. It may be suitable for electromagnetic suppression in the scanned frequency range. The attenuation coefficient or specific shielding efficiency is the more appropriate parameter to check the suitability of any material for EMI shielding. This coefficient defines the absorptive shielding efficiency per unit thickness. Fig. 7.11(d) shows that the

attenuation coefficient increases with frequency, and doping enhance the specific shielding efficiency continuously.

Table 7.5 Values of electromagnetic and shielding parameters of the sintered $Ba_{2-x}La_xCo_{2-x}Mg_xFe_{12}O_{22}$ ($0 \leq x \leq 0.5$) ferrite samples at different frequencies.

Frequency (GHz)	Parameters	x = 0.0	x = 0.1	x = 0.2	x = 0.3	x = 0.4	x = 0.5
12.5		0.356	0.431	0.783	1.289	1.146	1.489
14.5	μ'	0.234	0.286	0.369	1.306	1.143	1.365
16.5		0.154	0.381	0.341	1.069	1.010	1.263
12.5		0.099	0.347	0.356	0.257	0.296	0.239
14.5	μ''	0.446	0.394	0.405	0.479	0.319	0.112
16.5		0.629	0.454	0.494	0.453	0.261	0.079
12.5		0.234	0.519	0.266	7.970	7.079	5.325
14.5	ε'	1.046	1.622	1.352	7.090	6.814	5.867
16.5		2.224	1.954	2.184	8.145	6.926	3.907
12.5		0.719	0.928	0.837	1.120	0.529	1.537
14.5	ε''	1.273	1.786	1.744	0.390	0.467	1.855
16.5		1.055	1.687	1.332	0.752	0.809	1.272
12.5		2.596	3.103	3.437	2.645	2.620	2.238
14.5	SE_R (dB)	1.473	1.767	1.396	1.604	1.398	1.214
16.5		1.608	1.823	1.431	1.590	1.494	1.330
12.5		13.051	13.445	12.358	10.745	9.890	8.968
14.5	SE_A (dB)	18.674	18.699	18.854	14.178	11.548	10.135
16.5		26.545	24.302	24.503	15.873	12.952	11.316
12.5		15.646	16.547	15.795	13.390	12.510	11.297
14.5	SE_T (dB)	20.146	20.467	20.251	15.782	12.946	11.348
16.5		28.153	26.124	25.934	17.464	14.447	12.646
12.5		0.730	0.930	0.785	1.054	0.465	1.444
14.5	σ_{ac}(S/cm)	1.499	2.076	1.899	0.426	0.476	2.023
16.5		1.416	2.233	1.652	0.935	0.940	1.580

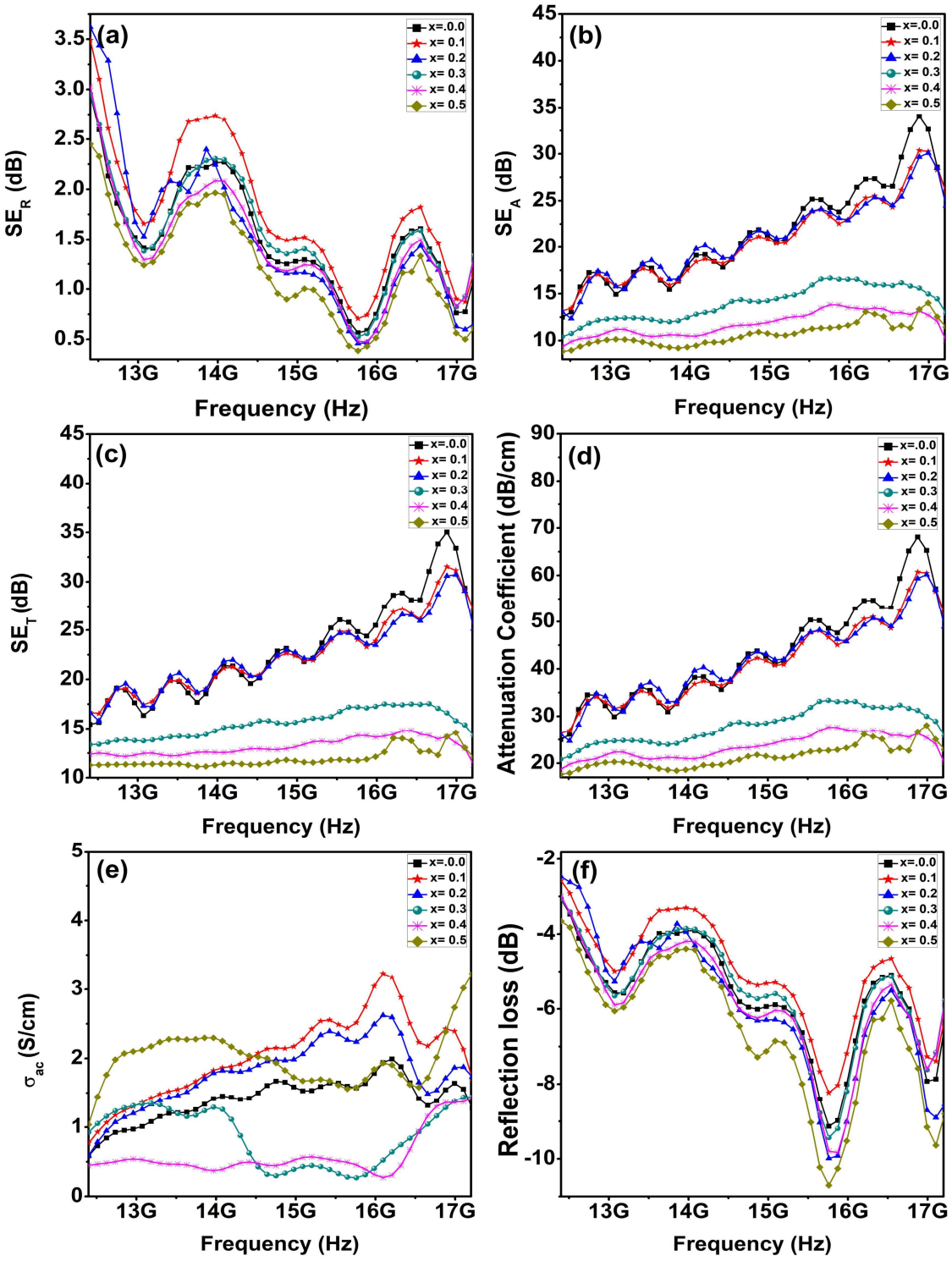

Figure 7.11 Frequency dependence (a) SE_R, (b) SE_A, (c) SE_T, (d) attenuation coefficient, (e) σ_{ac}, and (f) R_L of sintered $Ba_{2-x}La_xCo_{2-x}Mg_xFe_{12}O_{22}$ ($0 \leq x \leq 0.5$) ferrite samples.

The ac electrical conductivity for the samples is found by using the relation

$$\sigma_{ac} \approx 2\pi f \varepsilon_o \varepsilon'' \quad (7.5)$$

and tabulated in Table 7.5. It is observed that all the substituted samples have higher electrical conductivity excepting x = 0.3 and 0.4 compositions. The rising electrical conductivity behavior may be due to the SE_T response of the materials [(Chandra Babu Naidu, Roopas Kiran, and Madhuri, 2017)]. It is obvious that when a hexaferrite sample is placed in the transmission line, a portion of the incident energy gets reflected. This part of the energy can be quantified as return or reflection losses for that material [(Joseph *et al.*, 2013)]. The frequency-dependent reflection losses (R_L) can be estimated using the following relation;

$$R_L = -20 \log S_{11} \quad (7.6)$$

Fig. 7.11(f) shows the deviation of the reflection losses with frequency for the sample having a thickness of 5 mm. All the samples show optimum reflection losses varying from -2.0 dB to -10.7 dB within the scanned frequency range. For microwave absorption purposes, the material should ensure a low reflection loss [(Shams Alam *et al.*, 2016)]. Fig. 7.11(f) shows that all the samples show four resonating peaks at 13.07, 14.86, 15.76, and 17.10 GHz, respectively. The best value of reflection losses among all the synthesized samples is obtained as -10.70 dB in x = 0.5 substituted 5 mm sample with a bandwidth from 15.6 GHz to 15.8 GHz. This obtained value is much higher than the previously reported literature for a 5 mm sample within Ku-band frequency [(Song *et al.*, 2016)]. It can absorb 90% of the incident microwave in this particular frequency range [(Yusmaniar *et al.*, 2021)]. This enhancement of R_L performance may be ascribed due to an increase in porosity. As the pores increase, the microwave can penetrate more effectively due to fewer direct reflections on the surface of the substituted barium hexaferrite [(Ahmed *et al.*, 2020)]. It can also be elucidated due to the increasing anisotropy, including shape

anisotropy and magneto-crystalline anisotropy of the material. Consequently, the other parameters, i.e., the presence of soft ferrite impurity phases and reduced grain size, the presence of unsaturated coordination, and dangled bonds on the surface, may cause the enhancement of manifold scattering and interface polarization, which makes $Ba_{1.5}La_{0.5}Co_{1.5}Mg_{0.5}Fe_{12}O_{22}$ a promising absorbing material in the Ku-band.

7.3 Summary

The nanocrystalline La–Mg substituted Y-type barium hexaferrites are synthesized using the sol-gel auto combustion route. X-ray diffraction, FTIR spectra, and SEM analysis establish the formation of the hexaferrite samples with impurity phases. The magnetic measurements reveal that the saturation magnetization decreases, and the coercivity increases with increasing La^{3+} and Mg^{2+} content. The substituted sample $Ba_{1.5}La_{0.5}Co_{1.5}Mg_{0.5}Fe_{12}O_{22}$ shows the best reflection loss and total shielding effectiveness with absorption as a dominant shielding mechanism within the scanned frequency range. The improved shielding effectiveness for the $Ba_{1.5}La_{0.5}Co_{1.5}Mg_{0.5}Fe_{12}O_{22}$ hexaferrite sample can be proposed as an excellent microwave absorber material within the Ku-band (12.5 to 17.5 GHz) of the frequency with a moderate reflection loss (R_L<-10dB).